Insulator-metal-superconductor transition in the medium-entropy van der Waals compound $MPSe_3$ (M = Fe, Mn, Cd, and In) under high pressure

Xu Chen,[1,*] Junjie Wang,[1,2,*] Tianping Ying,[1,†] Dajian Huang,[3] Huiyang Gou,[3] Qinghua Zhang,[1] Yanchun Li,[4] Hideo Hosono,[5] Jian-gang Guo,[1,6,‡] and Xiaolong Chen[1,6,§]

[1]*Beijing National Laboratory for Condensed Matter Physics, Institute of Physics, Chinese Academy of Sciences, Beijing 100190, China*
[2]*University of Chinese Academy of Sciences, Beijing 100049, China*
[3]*Center for High Pressure Science and Technology Advanced Research (HPSTAR), Beijing 100094, China*
[4]*Beijing Synchrotron Radiation Facility Institute of High Energy Physics, Chinese Academy of Sciences, Beijing 100049, China*
[5]*Materials Research Center for Element Strategy, Tokyo Institute of Technology, Yokohama 226-8503, Japan*
[6]*Songshan Lake Materials Laboratory, Dongguan, Guangdong 523808, China*

(Received 12 July 2022; revised 18 October 2022; accepted 19 October 2022; published 2 November 2022)

MPX_3 (M = metals; X = S or Se) represents a large family of van der Waals (vdW) materials featuring P-P dimers of ∼2.3 Å separation. A dramatic alteration of its electrical transport properties, such as metal-insulator transition, has not been realized by intentional chemical doping and ionic intercalation. Here, we employ an entropy-enhancement strategy to successfully obtain a series of medium-entropy $MPSe_3$ (M = Fe, Mn, Cd, and In), in which the electrical and magnetic properties change simultaneously. Lone-pair electrons of P emerge due to the dissociation of the dimers as evidenced by a 35% elongation in the P-P interatomic distance. The band gap widens from 0.1 to 0.7 eV by this dissociation. Under external physical pressure up to ∼50 GPa, a giant collapse of up to 15% in the c axis happens, which is in contrast to the in-plane shrinkage of their counterparts Fe/$MnPSe_3$. It leads to the recombination of P^{3-} with lone-pair electrons into a P-P dimer and the smallest bulk modulus of 28 GPa in MPX_3. The medium-entropy $MPSe_3$ transitions from a spin-glass insulator to metal, and to superconductor, which is rarely observed in MPX_3. Our findings highlight the P-P dimer as an indicator to probe diverse electronic structure and the effectiveness of entropy enhancement in materials science.

DOI: 10.1103/PhysRevB.106.184502

I. INTRODUCTION

Atomic dimers are pairs of atoms connected by covalent or metallic bonds, which can adopt or release electrons, acting as a charge reservoir. The elongation or shortening of bond length in a dimer often leads to change in crystal structure accompanying different electron concentrations and magnetism in compounds [1,2]. Typical dimers include Te-Te, O-O, and As-As, as well as metallic bonds Mn-Mn and Ir-Ir. It is reported that the charge redistribution in the interlayer Ir-Ir dimer of $IrTe_2$ is controlled by the interlayer Te-Te dimer, which is believed to be a critical factor for determining charge density wave and superconductivity (SC) [3]. Meanwhile, in Pt- and Pd-doped $IrTe_2$, SC is induced as a result of decoupling the interlayer Te-Te dimers [4,5]. In an O-O dimer, the π^* orbital with unpaired electrons endows its magnetic ordering, and diverse p-electron magnetic properties are observed in Rb_4O_6, and α-$BaNaO_4$ due to the differently charged O_2^- or $O_2^{1.5-}$ dimers [6–9]. In $LaFe_2As_2$, a collapsed to uncollapsed phase transition caused by breaking the interlayer As-As dimer is intimate to the emergence of SC [10].

MPX_3 (M = divalent metal; X = S, Se) represents a large family of magnetic van der Waals (vdW) compounds, which exhibit diverse properties in fundamental and applied research [11–15]. The magnetic M^{2+} ions occupy a honeycomb lattice; thus the isolated monolayer MPX_3 is dubbed "magnetic graphene" with large magnetic anisotropic energy [16–20]. Apart from transition metals, M ions can be alkaline-earth metal (Ae^{II}) in $MgPSe_3$, a mixture of +1 (A^I) and +3 cations (RE^{III}) in $Ag^I In^{III} P_2Se_6$, and partially occupied M^{III} cation in $(Ga^{III})_{2/3} PSe_3$ [21–24]. The sum of the chemical valence of M should be +2 so as to keep charge neutrality. SC has long been anticipated in the MPX_3 system, but so far, it has only been observed in $FePSe_3$ under external pressure (8 GPa) with a transition temperature (T_c) of 4 K [11]. It is proposed that the switch of high spin to low spin in the Fe $3d^6$ electron induces magnetic-nonmagnetic transition, which is crucial for realizing SC. This explanation is supported by the absence of SC in $MnPSe_3$ with odd d-electron number ($3d^5$) under pressure [25], but disputed by a recent neutron diffraction study on the pressurized $FePSe_3$, which reveals that the local magnetic moment survives with $\sim 5\mu_B$/Fe in the whole pressure range [26]. The picture of spin crossover may not directly explain the SC in $FePSe_3$.

Despite the variety of M ions, the P-P distance always lies around 2.3 Å, suggesting a robust nature of the P-P dimer in MPX_3. Field gating, chemical doping, and molecular intercalation all failed to change the semiconducting or insulating

*These authors contributed equally to this work.
†ying@iphy.ac.cn
‡jgguo@iphy.ac.cn
§chenx29@iphy.ac.cn

 ©2022 American Physical Society

behavior in MPX_3 and the reason is not clear so far. Here, we use an entropy strategy to alloy multiple elements in $MPSe_3$ (M = Fe, Mn, Cd, and In), which introduces extra electrons leading to breaking the P-P dimer. Here, we report the control of P-P distance in the MPX_3 system with a 35% elongation from 2.3 to 3.1 Å. Under external pressure, the lone pairs generated from the breaking P-P bonds recombine with each other into a P-P dimer, accompanied by an abrupt collapse of the c axis, rather than the ab plane as reported in $FePX_3$ and $MnPX_3$. Accordingly, the medium-entropy $MPSe_3$ undergoes an insulator-metal-superconductor transition.

II. METHODS

A. Synthesis

Single-crystalline medium-entropy $MPSe_3$ was grown by using the chemical vapor transport (CVT) method. A quartz tube was kept at a high temperature of 900 K and a low temperature of 650 K. After holding the temperatures for 1 week, the single crystals were obtained after quenching the quartz tube in ice water. I_2 was used as the transport agent.

B. Characterization

Powder x-ray diffraction (PXRD) patterns of samples were collected at room temperature using a Panalytical diffractometer with Cu $K\alpha$ (λ = 1.5408 Å) radiation. The composition of the sample was determined by energy dispersive spectroscopy (EDS). High-resolution transmission electron microscope (HRTEM) and EDS mapping were taken using an ARM-200F (JEOL, Tokyo, Japan) scanning transmission electron microscope (STEM) operated at 200 kV with a CEOS Cs corrector (CEOS GmbH, Heidelberg, Germany) to cope with the probe-forming objective spherical aberration. The x-ray photoemission spectrum (XPS) was taken at room temperature. Electrical resistance (ρ) and DC/AC magnetic susceptibility (χ) were measured through the physical property measurement system (PPMS, SVS, Quantum Design).

The high-pressure transport property of medium-entropy $MPSe_3$ was measured in a physical property measurement system (PPMS, Quantum Design) by using a diamond anvil cell (DAC) with a facet diameter of 300 μm. The four-wire method in a Be-Cu cell was used for the resistance (R) measurements. Cubic boron nitride (cBN) powders were employed as the pressure transmitting medium and the insulating material. The pressure was calibrated using ruby fluorescence at room temperature. Synchrotron XRD patterns were collected at the Beamline 4W2 at the Beijing Synchrotron Radiation Facility (λ = 0.6199 Å). The beam sizes were 15 and 5 μm at the bending and undulator beamlines, respectively.

III. RESULTS AND DISCUSSION

We tried to alloy metals such as Fe, Mn, Cr, Co, Zn, Cd, and In at the Fe site of $FePSe_3$, and found only the combination of Fe, Mn, Cd, and In produced single-phase samples. In Figs. S1 and S2 of the Supplemental Material [27], samples with different entropy are synthesized with the nominal composition of $FePSe_3$, $Fe_{0.8}Mn_{0.1}Cd_{0.05}In_{0.05}PSe_3$, $Fe_{0.7}(MnCd)_{0.1}In_{0.1}PSe_3$, and $(FeMnCd)_{0.25}In_{0.17}PSe_3$, and

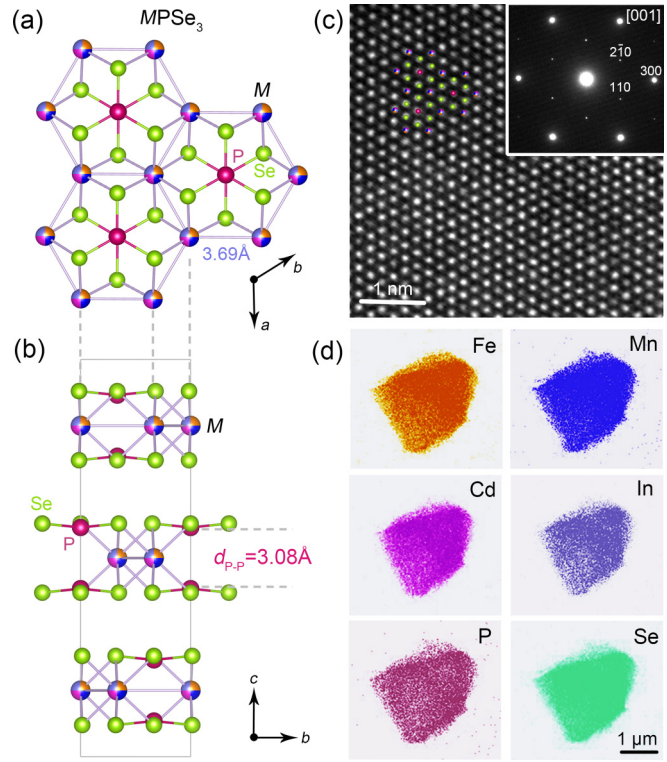

FIG. 1. (a), (b) Top and side view of $(FeMnCd)_{0.25}In_{0.17}PSe_3$ along the c axis and a axis. (c) HRTEM image of $(FeMnCd)_{0.25}In_{0.17}PSe_3$ taken along the c axis. Inset is indexed SAED (selected area electron diffraction) image. (d) EDS mapping of Fe (orange), Mn (blue), Cd (magenta), In (purple), P (brown), and Se (green) of $(FeMnCd)_{0.25}In_{0.17}PSe_3$. The scale bar is 1 μm.

are referred to as $Fe_{1.0}$, $Fe_{0.8}$, $Fe_{0.7}$, and $Fe_{0.25}$ as a shorthand notation. Figures 1(a) and 1(b) illustrate the crystal structure of $MPSe_3$, where M is a mixture of Mn, Fe, Cd, and In. The M atoms are octahedrally coordinated by six Se atoms that are then covalently bonded to P-P dimers, forming an ethanelike $(P_2Se_6)^{4-}$ cluster [28–30]. In the $Fe_{0.25}$ sample, the M-M distance is 3.69 Å, longer than the Fe-Fe of 3.44 Å and Mn-Mn of 3.50 Å in $FePSe_3$ and $MnPSe_3$, respectively [11,25]. The HRTEM image of the $Fe_{0.25}$ sample reveals good crystallinity with partial M vacancies; see Fig. 1(c). The EDS mapping of the $Fe_{0.25}$ sample is shown in Fig. 1(d), indicating a homogeneous elemental distribution of the alloyed elements. Rietveld refinement of all the PXRD patterns of $FePSe_3$ and three medium-entropy $MPSe_3$ samples can be found in Fig. 2, with the refinement results summarized in Table I. Because the ionic radii of Mn (0.67 Å), Cd (0.95 Å), and In (0.80 Å) are larger than that of Fe (0.61 Å), the diffraction peaks systemically shift to lower angles as the content of the dopants increases, suggesting that these atoms have been successfully incorporated at the Fe site.

Figure 3 shows the evolution of the structure and physical property of four samples. The lattice constants a and c of four samples are plotted in Fig. 3(a). By increasing the content of dopants, the a axis increases from 6.26 to 6.38 Å, and the c axis increases from 19.8 to 20.0 Å. The expansion of the c axis is mainly caused by the enlargement of P-P distances as shown in Fig. 3(b). In the $Fe_{0.25}$ sample, the P-P distance

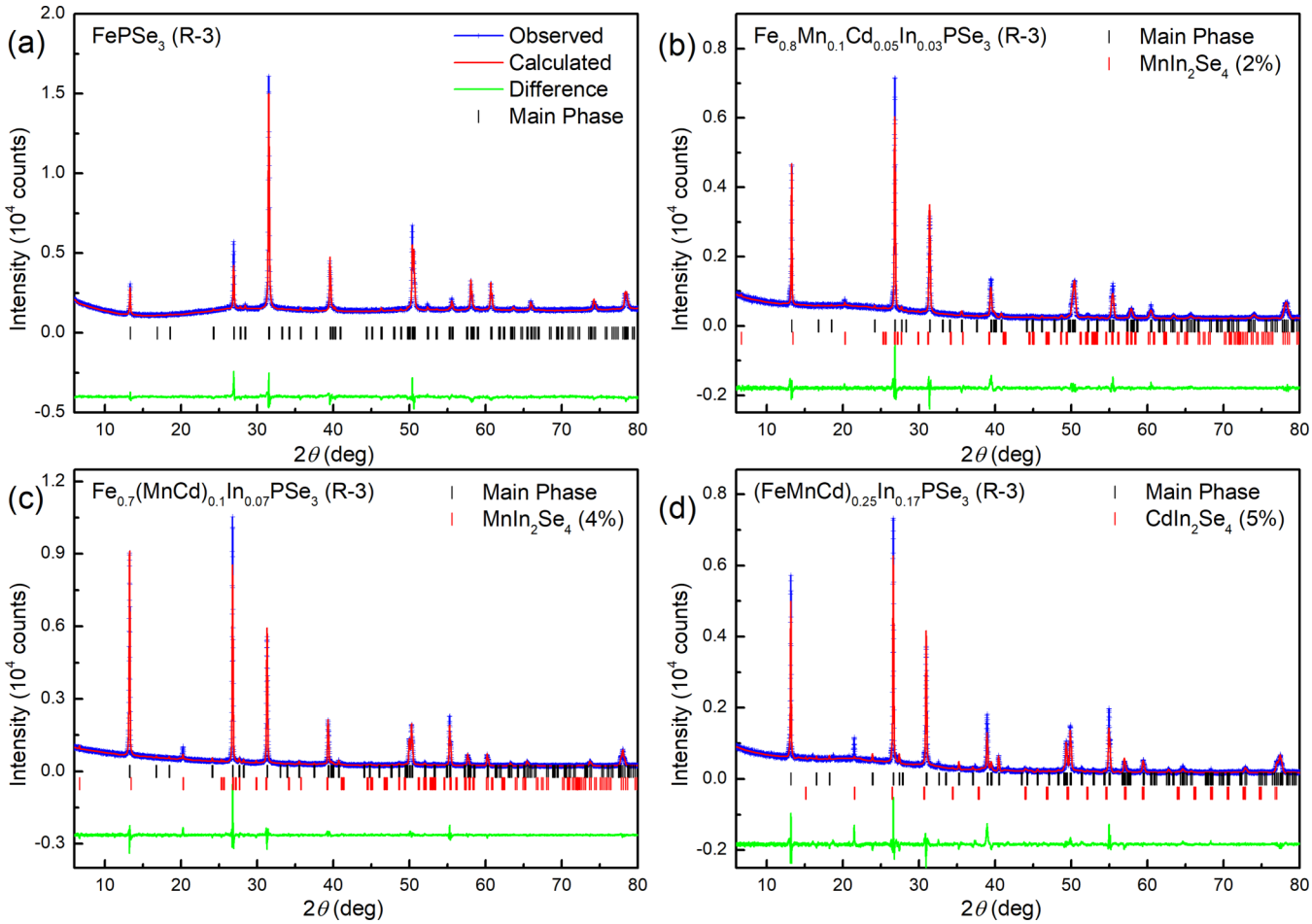

FIG. 2. Rietveld refinements of PXRD patterns collected at ambient pressure of (a) $FePSe_3$, (b) $Fe_{0.8}Mn_{0.1}Cd_{0.05}In_{0.03}PSe_3$, (c) $Fe_{0.7}(MnCd)_{0.1}In_{0.07}PSe_3$, and (d) $(FeMnCd)_{0.25}In_{0.17}PSe_3$. Minor phase of $MnIn_2Se_4$ was detected.

is 3.08 Å, which considerably exceeds ∼2.3 Å, the typical P-P dimer region. The electrical resistivity versus temperature (ρ-T) curves of four samples indicate they are semiconductors as shown in Fig. S3 of the Supplemental Material [27]. The fitted thermally activated gaps (E_a) are plotted in Fig. 3(b). The E_a increases from 0.1 eV in $FePSe_3$ to 0.7 eV in $Fe_{0.25}$. We show the XPS of anion P in Figs. 3(c). The redshifts of P's $2p_{5/2}$ and $2p_{3/2}$ peaks indicate that the valences of P

TABLE I. Crystallographic parameters of $FePSe_3$ and three medium-entropy $MPSe_3$ samples with an R-3 space group.

Compound	$FePSe_3$	$Fe_{0.8}Mn_{0.1}Cd_{0.05}In_{0.03}PSe_3$	$Fe_{0.7}(MnCd)_{0.1}In_{0.07}PSe_3$	$(FeMnCd)_{0.25}In_{0.17}PSe_3$
a (Å)	6.2622 (1)	6.2871 (3)	6.3059 (1)	6.3841 (2)
c (Å)	19.8114 (6)	19.8590 (9)	19.8966 (4)	20.0074 (8)
V (Å^3)	672.82 (3)	679.81 (5)	685.18 (3)	706.19 (5)
P-P (Å)	2.35 (2)	2.53 (2)	2.55 (2)	3.08 (2)
R_p	2.74%	5.26%	4.93%	6.48%
R_{wp}	3.73%	7.37%	6.82%	9.43%
R_{expt}	2.51%	4.79%	4.66%	4.90%
χ^2	2.21	2.37	2.14	3.70
Atomic parameters:				
Fe/M(1)	(0, 0, 0.1667)	(0, 0, 0.1667)	(0, 0, 0.1667)	(0, 0, 0.1667)
P(1)	[0, 0, 0.4408(5)]	[0, 0, 0.4363(5)]	[0, 0, 0.4359(9)]	[0, 0, 0.4230(7)]
Se(1)	[0.3333, 0.0124(6) 0.0825(2)]	[0.3333, 0.0153(9) 0.0807(1)]	[0.3333, 0.0075(8) 0.0833(1)]	[0.3333, 0.0146(9) 0.0797(1)]

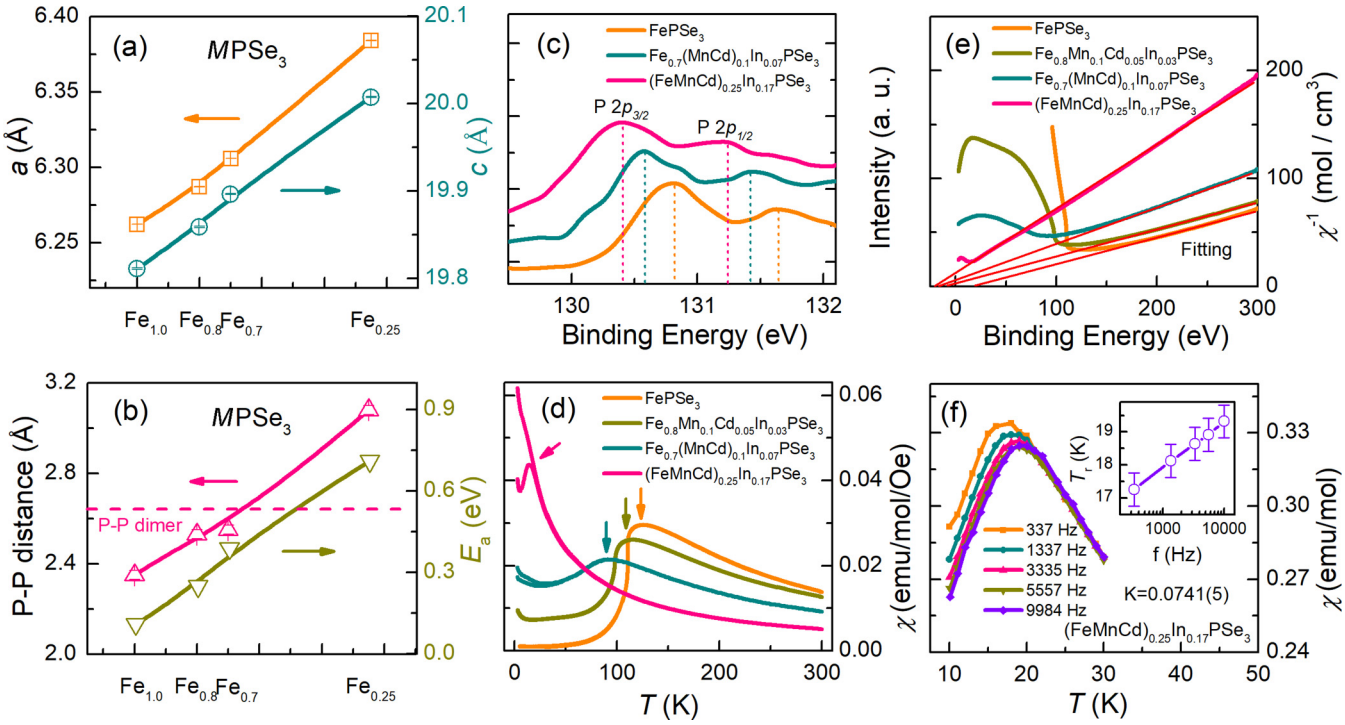

FIG. 3. (a) Lattice constants a and c of $FePSe_3$ and three medium-entropy $MPSe_3$ samples. (b) P-P distance and band gap (E_a) estimated from temperature dependence of conductivity in four samples. (c) P $2p$ XPS of three samples. (d), (e) DC susceptibility (χ) and $1/\chi$ of four samples as a function of temperature from 2 to 300 K. (f) AC susceptibility of $(MnFeCd)_{0.25}In_{0.17}PSe_3$ under different frequencies. Inset is frequency-dependent freeze temperature (T_r). Solid lines are fitting curves based on equation of $K = \Delta T_f/(T_f\,\Delta\log f)$. The obtained $K = 0.0741(5)$ falls into the range of $0.0045 \leqslant K \leqslant 0.08$ for canonical spin-glass systems.

qualitatively become more negative. It suggests the formation of partial P^{3-} lone-pair electrons by breaking of P-P dimers as the dopants are increased.

Temperature-dependent DC magnetic susceptibility (χ-T) under zero-field cooling and field cooling modes of $FePSe_3$ and three medium-entropy $MPSe_3$ samples are plotted in Figs. 3(d) and 3(e), and Fig. S4 of the Supplemental Material [27]. The Néel temperature (T_N) of 122 K in $FePSe_3$ is suppressed to a spin-glass-like transition of 15 K in the $Fe_{0.25}$ sample. Fitting the data above T_N by the Curie-Weiss equation yields effective magnetic moments $\mu_{eff} = 5.6(1)\mu_B$, $5.5(1)\mu_B$, $4.9(1)\mu_B$, and $3.7(1)\mu_B$ for $Fe_{1.0}$, $Fe_{0.8}$, $Fe_{0.7}$, and $Fe_{0.25}$ samples, respectively. As averaged to magnetic ions (Fe and Mn), the effective magnetic moment is $\sim 5.5\mu_B$. With the increase of dopants, the fitted Weiss temperatures (T_θ) change from positive to negative, indicating a transition of local spin interaction from ferromagnetic to antiferromagnetic interactions. We further measured the temperature-dependent AC magnetic susceptibility from 10 to 30 K under different frequencies. The peak of $T_r \sim 15$ K shifts to higher temperature with increasing frequency f, which is a typical a canonical spin-glass behavior [Fig. 3(f)] [31].

We selected two typical samples, $Fe_{0.8}$ and $Fe_{0.25}$, to study the pressure-induced evolution structure and electrical transport properties. The collected PXRD patterns under pressures are shown in Figs. S5 and S6 of the Supplemental Material [27]. Figures 4(a) and 3(b) present pressure-dependent (113) and (300) peak shifts of $Fe_{0.8}$ and $Fe_{0.25}$. It can be found that both angles monotonously shift to higher values with increasing pressure, indicating shrinkage in the unit cell. At critical pressures of 12 GPa ($Fe_{0.8}$) and 28 GPa ($Fe_{0.25}$),

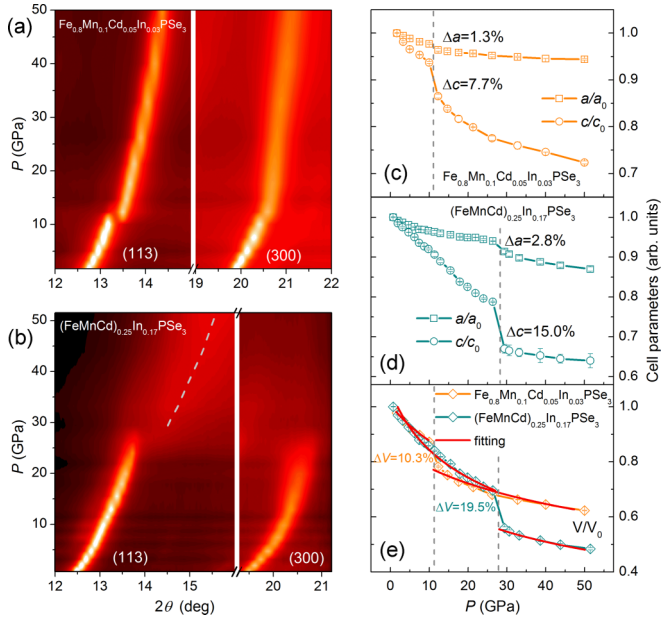

FIG. 4. (a), (b) Color contour of the (113) and (300) diffraction peaks for $Fe_{0.8}Mn_{0.1}Cd_{0.05}In_{0.05}PSe_3$ ($Fe_{0.8}$) and $(FeMnCd)_{0.25}In_{0.17}PSe_3$ ($Fe_{0.25}$) under external physical pressure. (c)–(e) Pressure-dependent lattice parameters and volume of unit cell for both samples.

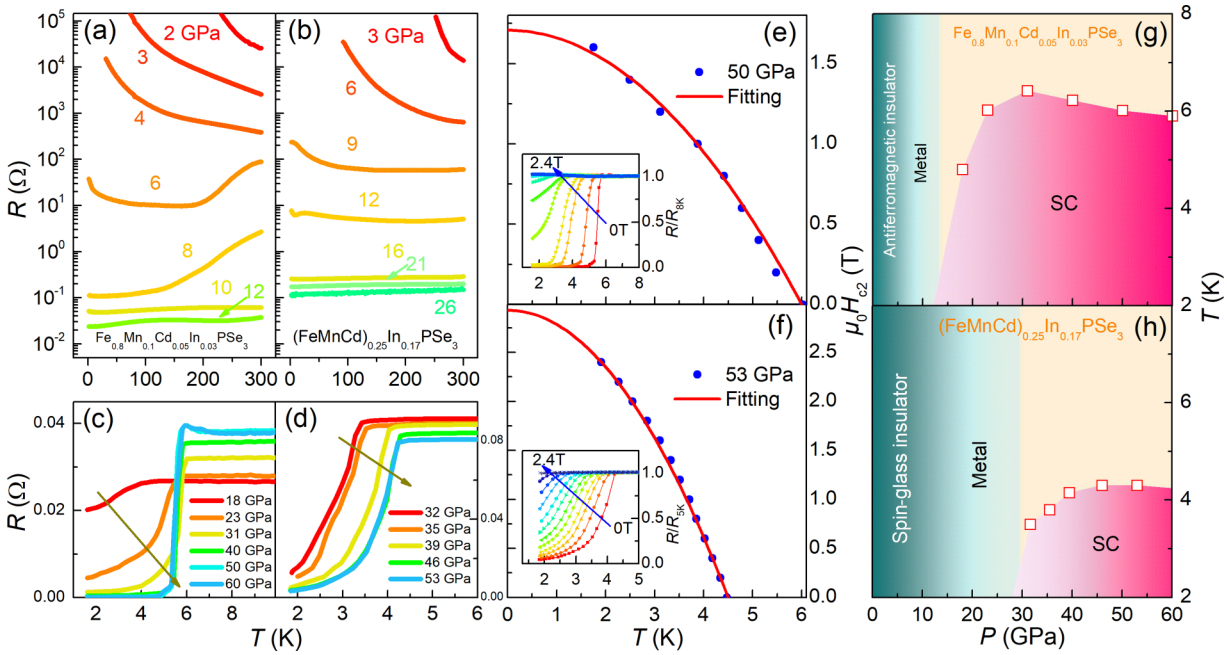

FIG. 5. (a), (c) Temperature dependence of R-T curves of $Fe_{0.8}$ below and above 12 GPa. (b), (d) Temperature dependence of R-T curves of $Fe_{0.25}$ below and above 26 GPa. Temperature-dependent upper critical fields of (e) $Fe_{0.8}$ at 50 GPa and (f) $Fe_{0.25}$ at 53 GPa. Fitting curves are GL equation shown in main text. Insets are temperature dependence of the normalized resistances, respectively. (g), (h) Electronic phase diagram of both samples versus pressure.

they undergo a kind of quasi-isostructural phase transition, accompanied with an abrupt decrement in lattice constants. To analyze the anisotropic compressibility of $FePX_3$, we refined the PXRD patterns of medium-entropy $MPSe_3$ using a trigonal space group R-3 [11,25]. The normalized lattice constants a and c against pressure are plotted in Figs. 4(c) and 4(d). For the $Fe_{0.8}$, the total shrinkage ratios of the a and c axes, i.e., $\Delta l = 100\%[l_{0\,\mathrm{GPa}}\text{-}l_{50\,\mathrm{GPa}}]/l_{0\,\mathrm{GPa}}$, are 5.5% and 28.0%, respectively. As the phase transition region is crossed, the collapse ratios of the a and c axes are 1.3% and 7.7%, respectively. In the $Fe_{0.25}$, the total shrinkage ratios a and c axis are 13.0% and 36.0%, and the collapse ratios of the a and c axes are 2.8% and 15.0%, respectively. As previously reported, the collapse ratio of Δa is ~4%, and that of Δc is zero in $FePSe_3$. The shrinkage is mostly restricted within the ab plane [11]. In our medium-entropy $MPSe_3$, the P-P distance lies far beyond the covalent bond length. Since the P-P bond is more compressive along the c axis, the primary effect under compression changes from in plane to out of plane. It is noteworthy that the giant shrinkage of 15% can lead to the recombination of the P-P dimer.

Figure 4(e) displays the plot of unit-cell volume (V) of $Fe_{0.8}$ and $Fe_{0.25}$ samples under pressure. The shrinkage ratios of V from ambient pressure to 50 GPa are 38% and 52%, and the collapse ratios at the phase transition pressure are 10.3% and 19.5%, respectively. We fitted the pressure-dependent V of both samples by using the third-order Birch-Murnaghan equation of state [32–34]:

$$P = \frac{3}{2}B[(V_0/V)^{7/3}-(V_0/V)^{5/3}] \times \left\{1+\frac{3}{4}(B'-4)[(V_0/V)^{2/3}-1]\right\},$$

where B is the average isothermal bulk modulus, B' (~4) the first pressure derivative of B, and V and V_0 the volume under pressure and zero-pressure volume. The fitted B_{LP} (B_{HP}) for the low- (high-) pressure phase $Fe_{0.8}$ and $Fe_{0.25}$ samples are 55(3)/78(9) GPa and 27(2)/28(8) GPa, respectively. The values of $Fe_{0.25}$ are very small for B in MPX_3 compounds; see Ref. [11]. In general, the B of a high-entropy alloy is higher than that of its individual components [35]. Based on our results, the B in layered compounds may be mainly determined by the strength and length of chemical bonds. Therefore, we suggest that the existence of soft P-P covalent bonds drastically reduces the B.

In Figs. 5(a) and 5(b), we can see that the resistance (R) is drastically reduced by 10^6 in magnitude with pressure. The semiconductor-metal transitions of $Fe_{0.8}$ and $Fe_{0.25}$ occur at 6 and 16 GPa, and the metallic state persists in the pressure range of 6-18 GPa and 1632 GPa, respectively. The enlargement of the low-temperature region is included in Fig. S7 of the Supplemental Material [27]. For both $Fe_{0.8}$ and $Fe_{0.25}$, a clear metal-insulating transition can be observed. The low-pressure curve shows a 3D variable-range hopping behavior (insets of Fig. 7). The competing nature of entropy-induced localization and pressure-driven itineration can be seen in the 8 GPa curve for $Fe_{0.8}$ and 12-16 GPa for $Fe_{0.25}$ at low temperature. Interestingly, once we fit all the metallic curves using the formula $R = R_0 + AT''$ (Fig. S8 of the Supplemental Material [27]) and extracted the coefficients in Fig. S9 of the Supplemental Material [27], peaks in A and dips in n at 12 and 27 GPa for $Fe_{0.8}$ and $Fe_{0.25}$ can be clearly seen, indicating the existence of quantum critical points on the verge of P-P dimer instabilities. The superconducting transitions in $Fe_{0.8}$ and $Fe_{0.25}$ are observed at $T_c = 4$ and 3.2 K, respectively, at pressures above 18 and 32 GPa; see Figs. 5(c) and 5(d). These

pressures are consistent with the critical pressures of structural collapse shown in Figs. 4(c) and 4(d). The maximal T_c of the $Fe_{0.8}$ sample is 6.2 K and then gradually decreases. For the $Fe_{0.25}$ sample, the T_c increases to 4.3 K at 46 GPa and then saturates. The upper critical fields $\mu_0 H_{c2}(0)$ are 1.7 T for the $Fe_{0.8}$ (50 GPa) and 2.9 T for the $Fe_{0.25}$ (53 GPa) according to Ginzburg-Landau fittin;, see Figs. 5(e) and 5(f). Their superconducting coherence lengths (ξ) are calculated to be 439 and 336 Å, respectively. Note that the SC originating from a spin-glass insulator is a rare case, which deserves detailed investigations on electronic structure.

$FePSe_3$ undergoes an in-plane collapse under external pressure, forming a pseudotrigonal monoclinic structure with intralayer Fe-Fe bonding [11]. This is reminiscent of the in-plane formation of the Ir-Ir dimer in CdI_2-type $IrTe_2$, where the charge redistribution between Ir-Ir and Te-Te regulates the CDW and SC [3]. In pyrite-type $IrSe_2$ and $IrTe_2$, on the other hand, the elongated Te-Te/Se-Se distances are responsible for the emergence of SC [36,37]. Similar behavior has been reported in the collapsed to uncollapsed transition in $LaFe_2As_2$ [10].

The status of the P-P dimers has also been reported in tuning magnetism. In $Sr_{1-x}Ca_xCo_2P_2$, the breaking of the P-P dimer is closely related to a transition from magnetic ($x = 1$) to nonmagnetic ($x = 0$) [38]. In $SrCo_2(Ge_{1-x}P_x)_2$, a ferromagnetic quantum critical point has been discovered on the verge of Ge(P)-Ge(P) dimer instability [39]. In our work, the collapse of the lone pair of P under high pressure triggers a transition from $(P_2)^{6-}$ to $(P\text{-}P)^{4-}$ and releases a certain amount of electrons. This charge redistribution significantly alters the electronic structure, i.e., increasing the carrier concentration and density of states at the Fermi level, in favor of SC [40–42].

IV. CONCLUSION

The P-P dimers are extremely flexible upon electron doping and under high pressure, which can act as a charge reservoir. We adopt a unique strategy by alloying multiple elements in medium-entropy $MPSe_3$ compounds, in which the breaking of the P-P dimer increases the electrical resistivity and activated gap. Under external physical pressure, the P-P dimers recombine as evidenced by the dramatic collapse of the c axis, which induces SC at the same time. It provides an effective way to tune the crystallographic and electronic structure of MPX_3. Our findings highlight the importance of synergistic entropy-driven and high-pressure effect in materials science.

ACKNOWLEDGMENTS

This work is financially supported by the National Key Research and Development Program of China (Grants No. 2018YFE0202600, No. 2017YFA0304700, and No. 2021YFA1401800), the National Natural Science Foundation of China (Grants No. 52272267, and No. 51922105), and Beijing Natural Science Foundation (Grant No. Z200005). ADXRD measurements were performed at 4W2 High Pressure Station, Beijing Synchrotron Radiation Facility (BSRF), which is supported by the Chinese Academy of Sciences (Grants No. KJCX2-SW-N20 and No. KJCX2-SW-N03).

[1] E. Kanda, T. Haseda, and A. Otsubo, Physica **20**, 131 (1954).
[2] T. C. Stamatatos, K. A. Abboud, W. Wernsdorfer, and G. Christou, Angew. Chem., Int. Ed. **47**, 6694 (2008).
[3] G. L. Pascut, K. Haule, M. J. Gutmann, S. A. Barnett, A. Bombardi, S. Artyukhin, T. Birol, D. Vanderbilt, J. J. Yang, S. W. Cheong, and V. Kiryukhin, Phys. Rev. Lett. **112**, 086402 (2014).
[4] A. F. Fang, G. Xu, T. Dong, P. Zheng, and N. L. Wang, Sci. Rep. **3**, 1153 (2013).
[5] J. J. Yang, Y. J. Choi, Y. S. Oh, A. Hogan, Y. Horibe, K. Kim, B. I. Min, and S. W. Cheong, Phys. Rev. Lett. **108**, 116402 (2012).
[6] R. J. Meier and R. B. Helmholdt, Phys. Rev. B **29**, 1387 (1984).
[7] G. D. Morris, J. H. Brewer, S. R. Dunsiger, and M. Montour, Hyperfine Interact. **104**, 381 (1997).
[8] S. Naghavi, S. Chadov, C. Felser, G. H. Fecher, J. Kübler, K. Doll, and M. Jansen, Phys. Rev. B **85**, 205125 (2012).
[9] J. Deng, J. G. Guo, and X. L. Chen, J. Am. Chem. Soc. **142**, 5234 (2020).
[10] A. Iyo, S. Ishida, H. Fujihisa, Y. Gotoh, I. Hase, Y. Yoshida, H. Eisaki, and K. Kawashima, J. Phys. Chem. Lett. **10**, 1018 (2019).
[11] Y. G. Wang, J. J. Ying, Z. Y. Zhou, J. L. Sun, T. Wen, Y. N. Zhou, N. N. Li, Q. Zhang, F. Han, Y. M. Xiao, P. Chow, W. G. Yang, V. V. Struzhkin, Y. S. Zhao, and H. K. Mao, Nat. Commun. **9**, 1914 (2018).
[12] R. Sogabe, Y. Goto, and Y. Mizuguchi, Appl. Phys. Express **11**, 053102 (2018).
[13] Y. Mizuguchi, J. Phys. Soc. Jpn. **88**, 124708 (2019).
[14] T. P. Ying, T. X. Yu, Y. S. Shiah, C. H. Li, J. Li, Y. P. Qi, and H. Hosono, J. Am. Chem. Soc. **143**, 7042 (2021).
[15] R. Wang, J. Z. Huang, X. H. Zhang, J. C. Han, Z. H. Zhang, T. L. Gao, L. L. Xu, S. W. Liu, P. Xu, and B. Song, ACS Nano **16**, 3593 (2022).
[16] P. A. Joy and S. Vasudevan, Phys. Rev. B **46**, 5425 (1992).
[17] P. G. Lacroix, R. Clement, K. Nakatani, J. Zyss, and I. Ledoux, Science **263**, 658 (1994).
[18] N. Sivadas, M. W. Daniels, R. H. Swendsen, S. Okamoto, and D. Xiao, Phys. Rev. B **91**, 235425 (2015).
[19] X. Zhang, X. D. Zhao, D. H. Wu, Y. Jing, and Z. Zhou, Adv. Sci. **3**, 1600062 (2016).
[20] C. C. Mayorga-Martinez, Z. Sofer, D. Sedmidubský, Š. Huber, A. Y. S. Eng, and M. Pumera, ACS Appl. Mater. Interfaces **9**, 12563 (2017).
[21] J. A. Aitken, M. Evain, L. Iordanidis, and M. G. Kanatzidis, Inorg. Chem. **41**, 180 (2002).
[22] T. J. McCarthy and M. G. Kanatzidis, Inorg. Chem. **34**, 1257 (1995).

[23] M. A. Susner, M. Chyasnavichyus, M. A. McGuire, P. Ganesh, and P. Maksymovych, Adv. Mater. **29**, 1602852 (2017).
[24] M. A. McGuire, T. K. Reynolds, and F. J. DiSalvo, Chem. Mater. **17**, 2875 (2005).
[25] Y. G. Wang, Z. Y. Zhou, T. Wen, Y. N. Zhou, N. N. Li, F. Han, Y. M. Xiao, P. Chow, J. L. Sun, M. Pravica, A. L. Cornelius, W. G. Yang, and Y. S. Zhao, J. Am. Chem. Soc. **138**, 15751 (2016).
[26] M. J. Coak, D. M. Jarvis, H. Hamidov, A. R. Wildes, J. A. M. Paddison, C. Liu, C. R. S. Haines, N. T. Dang, S. E. Kichanov, B. N. Savenko, S. Lee, M. Kratochvílová, S. Klotz, T. C. Hansen, D. P. Kozlenko, J.-G. Park, and S. S. Saxena, Phys. Rev. X **11**, 011024 (2021).
[27] See Supplemental Material at http://link.aps.org/supplemental/10.1103/PhysRevB.106.184502 for detailed measurements of PXRD patterns, energy dispersive spectroscopy, electrical resistivity, magnetic susceptibility, eynchrotron *in situ* XRD patterns, *A* coefficients, and temperature coefficient *n* of $MPSe_3$.
[28] Y. Zheng, X. X. Jiang, X. X. Xue, J. Dai, and Y. Feng, Phys. Rev. B **100**, 174102 (2019).
[29] H.-S. Kim, K. Haule, and D. Vanderbilt, Phys. Rev. Lett. **123**, 236401 (2019).
[30] B. L. Chittari, Y. Park, D. Lee, M. Han, A. H. MacDonald, E. Hwang, and J. Jung, Phys. Rev. B **94**, 184428 (2016).
[31] J. A. Mydosh, *Spin Glasses: An Experimental Introduction* (Taylor & Francis, London, 1993).
[32] F. Birch, and J. Geophys. Res.: Solid Earth **83**, 1257 (1978).
[33] H. X. Chen, D. L. Yang, Q. H. Zhang, S. F. Jin, L. W. Guo, J. Deng, X. D. Li, and X. L. Chen, Angew. Chem., Int. Ed. **58**, 4576 (2019).
[34] J. Guo, G. C. Lin, S. Cai, C. Y. Xi, C. J. Zhang, W. S. Sun, Q. L. Wang, K. Yang, A. Li, Q. Wu, Y. H. Zhang, T. Xiang, R. J. Cava, and L. L. Sun, Adv. Mater. **31**, 1807240 (2019).
[35] J. Huo, K. Li, B. Zang, M. Gao, L. M. Wang, B. Sun, M. Li, L. Song, J. Q. Wang, and W. H. Wang, Chin. Phys. Lett. **39**, 046401 (2022).
[36] Y. P. Qi, S. Matsuishi, J. G. Guo, H. Mizoguchi, and H. Hosono, Phys. Rev. Lett. **109**, 217002 (2012).
[37] J. G. Guo, Y. P. Qi, S. Matsuishi, and H. Hosono, J. Am. Chem. Soc. **134**, 20001 (2012).
[38] M. Imai, C. Michioka, H. Ohta, A. Matsuo, K. Kindo, H. Ueda, and K. Yoshimura, Phys. Rev. B **90**, 014407 (2014).
[39] S. Jia, P. Jiramongkolchai, M. R. Suchomel, B. H. Toby, J. G. Checkelsky, N. P. Ong, and R. J. Cava, Nat. Phys. **7**, 207 (2011).
[40] X. Chen, X. H. Zhan, X. J. Wang, J. Deng, X. B. Liu, X. Chen, J. G. Guo, and X. L. Chen, Chin. Phys. Lett. **38**, 057402 (2021).
[41] Y. T. Jia, C. S. Gong, Y. X. Liu, J. F. Zhao, C. Dong, G. Y. Dai, X. D. Li, H. C. Lei, R. Z. Yu, G. M. Zhang, and C. Q. Jin, Chin. Phys. Lett. **37**, 097404 (2021).
[42] Z. Y. Liu, Q. X. Dong, P. F. Shan, Y. Y. Wang, J. H. Dai, R. Jana, K. Y. Chen, J. P. Sun, B. S. Wang, X. H. Yu, G. T. Liu, Y. Uwatoko, Y. Sui, H. X. Yang, G. F. Chen, and J. G. Cheng, Chin. Phys. Lett. **37**, 047102 (2020).